Microscopic origin of the spin-reorientation transition in the kagome topological magnet $TbMn_6Sn_6$

Zhentao Huang,[1,*] Wei Wang,[2,*,†] Huiqing Ye,[3,*] Song Bao,[1] Yanyan Shangguan,[1] Junbo Liao,[1] Saizheng Cao,[3]
Ryoichi Kajimoto,[4] Kazuhiko Ikeuchi,[5] Guochu Deng,[6] Michael Smidman,[3,‡] Yu Song,[3,§] Shun-Li Yu,[1,7]
Jian-Xin Li,[1,7] and Jinsheng Wen[1,7,‖]

[1] *National Laboratory of Solid State Microstructures and School of Physics, Nanjing University, Nanjing 210093, China*
[2] *School of Science, Nanjing University of Posts and Telecommunications, Nanjing 210023, China*
[3] *Center for Correlated Matter and School of Physics, Zhejiang University, Hangzhou 310058, China*
[4] *J-PARC Center, Japan Atomic Energy Agency (JAEA), Tokai, Ibaraki 319-1195, Japan*
[5] *Neutron Science and Technology Center, Comprehensive Research Organization for Science and Society (CROSS), Tokai, Ibaraki 319-1106, Japan*
[6] *Australian Nuclear Science and Technology Organisation, Lucas Heights, NSW 2234, Australia*
[7] *Collaborative Innovation Center of Advanced Microstructures, Nanjing University, Nanjing 210093, China*

(Received 30 August 2023; revised 13 December 2023; accepted 11 January 2024; published 29 January 2024)

$TbMn_6Sn_6$ is a correlated topological magnet with a Mn-based kagome lattice, in which a Chern gap opens at the Dirac point at low temperatures. The magnetic moment direction of the ferrimagnetic order changes from in the kagome plane to out-of-plane upon cooling, which is essential for generating the Chern gap, but the underlying mechanism for the spin reorientation remains elusive. Here, we investigate the spin-reorientation transition in $TbMn_6Sn_6$ using neutron scattering. We provide direct evidence for the spin-reorientation transition and unveil the coexistence of two Tb modes at 200 K. To account for these results, we put forward a model based on SU(N) spin-wave theory, in which there is a temperature evolution of the ground state Tb $4f$ orbitals, driven by the crystalline electric field, single-ion anisotropy, and exchange interactions between Tb and Mn ions. Our findings shed light on the complex magnetism of $TbMn_6Sn_6$, despite its relatively simple ground state magnetic structure, and provide insights into the mechanisms for tuning magnetic topological materials.

DOI: 10.1103/PhysRevB.109.014434

I. INTRODUCTION

The kagome lattice is characterized by its network of corner-sharing triangles, and kagome Mott insulators have been studied extensively in the search for quantum-spin-liquid states stabilized by geometrically frustrated antiferromagnetic interactions [1,2]. More recently, interest in the kagome lattice has been extended to metals, which serve as a promising platform for investigating the interplay between geometry, topology, superconductivity, magnetism, and electronic correlations [3,4]. The electronic structures of the kagome lattice feature linearly dispersing bands that form Dirac crossings at the Brillouin zone corner, van Hove singularity saddle points at the Brillouin zone edge with a large density of states, and flat bands across the whole Brillouin zone [3,4]. These electronic states lead to fascinating physical consequences, including nontrivial electronic band topologies [5–12], unconventional superconductivity [13,14], strong correlations [15–18], competing charge and magnetic orders [19–23], and the anomalous Hall effect [24–29].

The aforementioned topologically nontrivial band structures and anomalous Hall effect can be found in the topological magnets RMn_6Sn_6 (R166, R is a rare-earth metal) [30–33], which consist of ferromagnetic kagome planes formed by Mn. They feature tunable magnetism that varies among members with different R ions. For example, Y166, Sc166 and Lu166 exhibit easy-plane antiferromagnetism, while Gd166, Er166, Tm166 and Yb166 display easy-plane ferromagnetism, and Dy166 and Ho166 are easy-cone ferromagnets [34–38]. These diverse magnetic configurations enable the exploration of a wide range of tunable topological phases and properties [39,40]. Within this family, $TbMn_6Sn_6$ stands out due to its simple collinear ferrimagnetic ground state with c-axis orientated moments and ideal Mn kagome layers [35,41,42]. The magnetic and crystal structures of $TbMn_6Sn_6$ which has the space group $P6/mmm$ and lattice constants $a = b = 5.5$ Å and $c = 9.0$ Å are illustrated in Fig. 1. Despite its simple magnetic structure, $TbMn_6Sn_6$ exhibits a complex magnetization process arising from the interplay of Mn kagome and Tb triangular layers [43–45], suggestive of competing magnetic interactions.

Recently, $TbMn_6Sn_6$ was reported to be a topological Chern-gapped Dirac metal resulting from the combined effect of spin-orbit coupling and the out-of-plane ferrimagnetic order [46]. It exhibits zero-field anomalous Hall, anomalous Nernst, and anomalous thermal Hall effects due to its out-of-plane magnetism and a large Berry curvature from the

---

[*] These authors contributed equally to the work.
[†] wwang@njupt.edu.cn
[‡] msmidman@zju.edu.cn
[§] yusong_phys@zju.edu.cn
[‖] jwen@nju.edu.cn

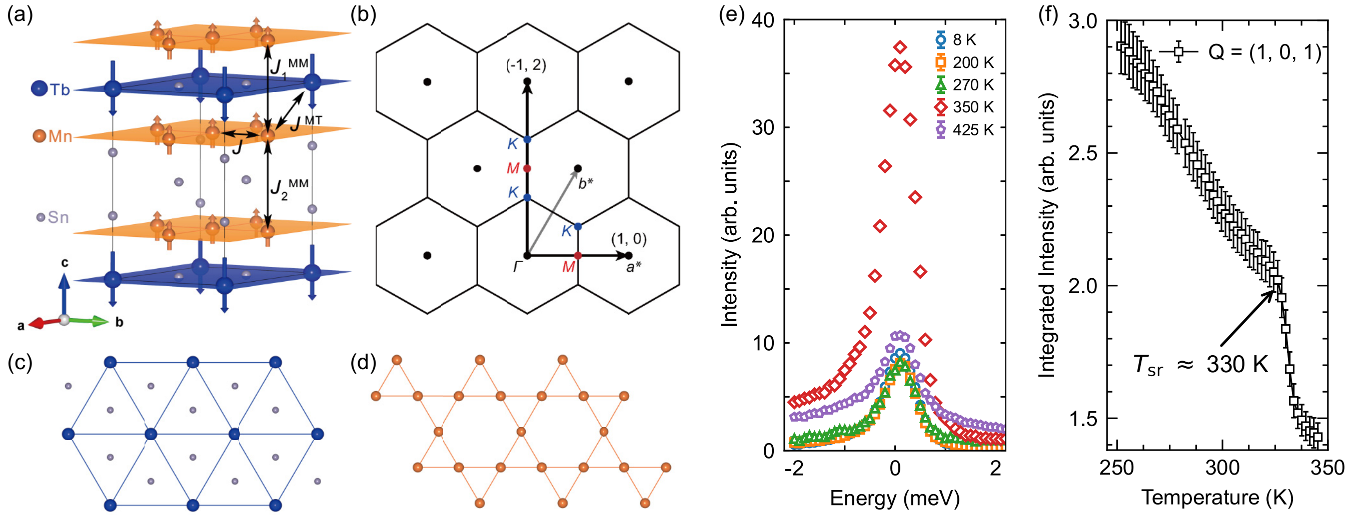

FIG. 1. (a) Schematic illustrations of the crystal and magnetic structures of $TbMn_6Sn_6$, drawn by VESTA [56]. Blue, orange and grey spheres represent Tb, Mn and Sn atoms, respectively. The main magnetic exchange paths are illustrated by the two-way arrows, including the couplings between Mn ions in the *ab*-plane (J), couplings between Mn and Tb layers (J^{MT}), as well as the couplings between different Mn layers (J_1^{MM} and J_2^{MM}). (b) Brillouin zone of the two-dimensional hexagonal lattice with reciprocal lattice vectors $\boldsymbol{a}^*$ and $\boldsymbol{b}^*$. High-symmetry points are labeled. (c) Diagram of the triangular lattice formed by Tb ions with Sn ions in the same layer. (d) Diagram of kagome lattice formed by Mn ions. (e) Elastic peak intensity of (0, 0, 1) at different temperatures, extracted from the 4SEASONS time-of-flight data. (f) Temperature dependence of the intensity at (1, 0, 1) measured using Taipan. The spin-reorientation temperature $T_{sr} \approx 330$ K is marked. Error bars represent one standard deviation throughout this work.

Chern-gapped Dirac fermions [7,39,47,48]. Intriguingly, a spin-reorientation transition occurs in $TbMn_6Sn_6$, where upon cooling the ordered spins rotate from the *ab* plane to the *c*-axis [35,41,42]. The spin-reorientation temperature T_{sr} is above room temperature and can be tuned by an external magnetic field [49]. Since the out-of-plane magnetic order that breaks time-reversal symmetry is a prerequisite for creating the Chern gap in $TbMn_6Sn_6$ [25,46,50], identifying the mechanism that drives the spin reorientation is crucial for comprehending the interplay between magnetism and electronic topology in $TbMn_6Sn_6$. The spin-reorientation transition may result from the competition between an easy-plane anisotropy of the Mn and a temperature-dependent uniaxial anisotropy of Tb [43,51–53]. In this scenario, increasing the temperature leads to enhanced fluctuations of the Tb moments that weaken the uniaxial anisotropy, eventually causing the moments to orient from out-of-plane to in-plane [54]. A possible role of Tb orbital states has also been discussed, whereby $TbMn_6Sn_6$ constitutes a two-state orbital alloy that has a temperature-dependent occupancy of different orbital states, and the spin-reorientation is induced when the orbital occupations reach a critical value [55].

In this work, we study the temperature evolution of the magnetic order and spin dynamics in $TbMn_6Sn_6$ using neutron scattering. By tracking the magnetic Bragg peak intensity as a function of temperature, we provide direct evidence for the spin-reorientation transition. Through inelastic neutron scattering (INS) measurements, we find that the Tb mode at 350 K (above T_{sr}) is different from that at 8 K, and at intermediate temperatures (200 K), there is a coexistence of two distinct Tb modes. We put forward a theoretical model based on SU(N) spin-wave theory that can well account for the temperature evolution of the magnetic excitations, in which the interplay of the crystalline electric field, single-ion anisotropy, and exchange interactions between Tb and Mn leads to a change of the Tb $4f$ ground state, driving the spin-reorientation transition in $TbMn_6Sn_6$.

II. EXPERIMENTAL DETAILS

Single crystals of $TbMn_6Sn_6$ were grown using a Sn self-flux method. A mixture of Tb (Aladdin 99.9% metals basis), Mn (Alfa Aesar 99.3% metals basis), and Sn (Aladdin 99.99% metals basis) powders were ground together in a molar ratio of $(TbMn_6)_{4.5}Sn_{95.5}$ and packed into an alumina crucible. The crucible was then sealed with a filter in a quartz ampoule under vacuum [57]. The ampoule was heated to 1000 °C over 25 hours and maintained at that temperature for 12 hours. The tube was then cooled to 620 °C at a rate of 2 °C per hour and quickly removed from the furnace, after which the flux was decanted using a centrifuge.

Elastic neutron scattering measurements were carried out using the Taipan thermal triple-axis spectrometer at ANSTO (Australian Nuclear Science and Technology Organisation), with samples aligned in the $(H, 0, L)$ scattering plane and E_f fixed to 14.87 meV. Time-of-flight INS measurements were performed using 4SEASONS (4D-Space Access Neutron Spectrometer) at J-PARC (Japan Proton Accelerator Research Complex) [58], operating in the multiple-E_i mode [59], with a set of $E_i = 50$ meV (primary) and 21 meV. The elastic energy resolutions were 2.37 and 0.84 meV, respectively, with a chopper frequency of 350 Hz. We coaligned 191 pieces of single crystals, weighing 3.7 g in total, using a Laue x-ray diffractometer and affixed them to aluminum holders using hydrogen-free adhesive. We set the $(H, 0, L)$ plane to be horizontal. The sample mosaic spread was 3.53° (full width at half maximum, FWHM) in the *ab* plane and 3.18° (FWHM) along the *c* axis, indicating a reasonable good sample coalignment. Data were collected by rotating the sample assembly about the [−120] axis from 30° to 180° in a step of 1°, with $\mathbf{k}_\mathrm{i} \parallel \mathbf{c}$ defined to be zero.

The wave vector $\boldsymbol{q}$ was expressed as (H, K, L) in reciprocal lattice units (rlu), with $(a^*, b^*, c^*) = (\frac{4\pi}{\sqrt{3}a}, \frac{4\pi}{\sqrt{3}b}, \frac{2\pi}{c})$ ($a = b = 5.5$ Å and $c = 9.0$ Å with space group $P6/mmm$). The INS data were analyzed using HORACE [60] and presented in terms of the orthogonal vectors [1, 0, 0], [−1, 2, 0], and [0, 0, 1], as illustrated in Fig. 1(b). The measured neutron scattering intensities are proportional to the spin-spin correlation function $S(\boldsymbol{q}, E) = \sum_{\alpha\beta}(\delta_{\alpha\beta} - \hat{q}_\alpha\hat{q}_\beta)S_{\alpha\beta}(\boldsymbol{q}, E)$, where E is the energy transfer and $\hat{q}_\alpha$ is the Cartesian component of the (unit) momentum transfer vector. The measured intensities were converted to the dynamic spin susceptibility via $\chi''(\boldsymbol{q}, E) = S(\boldsymbol{q}, E)[1 - \exp(-E/k_\mathrm{B}T)]$.

III. RESULTS

A. Neutron scattering

Figure 1(e) displays the energy scans through the (0, 0, 1) Bragg peak at different temperatures. The intensity at 350 K is significantly larger than those at 425 K (above $T_\mathrm{C} \approx 423$ K) and below $T_\mathrm{sr} \approx 330$ K. On the other hand, Fig. 1(f) shows a rapid drop in intensity of the (1, 0, 1) peak above around $T_\mathrm{sr} \approx 330$ K. These observations provide direct evidence that $\mathrm{TbMn_6Sn_6}$ experiences a spin-reorientation transition, with the spins evolving from being along the *c*-axis to lying in the *ab* plane upon increasing the temperature above T_sr, since neutrons are only sensitive to the spin component perpendicular to the momentum transfer. The spin-reorientation temperature T_sr is within the range of previously reported values [35,41–43,49,51–53].

We also investigated the spin excitations well below T_sr at 8 K, and above T_sr at 350 K. Considering the strong damping at high energies [44], we focus on the spin excitations below 50 meV. Figure 2 shows the spin excitation spectra measured at these two temperatures along different trajectories. All four panels were measured with $E_\mathrm{i} = 50$ meV. Figures 2(a) and 2(b) display the 8 K spectra along [H, 0, 2] and [0, 0, L], [H, 0, 3] and [1, 0, L], respectively. At base temperature (8 K), there are two modes at energies below 40 meV. As identified in Ref. [44], the relatively flat mode located at $E \approx 25$ meV with a bandwidth of about 5 meV corresponds to spin waves propagating in the Tb ions. This mode is denoted as the Tb mode, as shown in Figs. 2(a) and 2(b). The other more dispersive mode with a spin gap of around 7 meV is a Mn acoustic magnon mode. This mode has maximal structure factors in the Brillouin zones with even L, and so is labeled even mode [44].

Figures 2(c) and 2(d) display the spectra along the same directions as those in Figs. 2(a) and 2(b), respectively, but measured at 350 K. We find that the spin gap of the Mn even mode appears to be closed at 350 K. The other noticeable difference between the spectra measured at 8 and 350 K is that the relatively flat Tb mode around 25 meV disappears. Instead, there is a low-energy mode dispersing from the Γ point with a band top at about 8 meV. As 350 K is above T_sr, and the Tb spins all lie in the basal plane, this low-energy mode reflects the isotropic character of the Tb ions within the *ab* plane. Since the easy-axis anisotropy should weaken with increasing temperature, it is important to clarify whether the low-energy mode simply arises from the collapse of the anisotropy gap above T_sr.

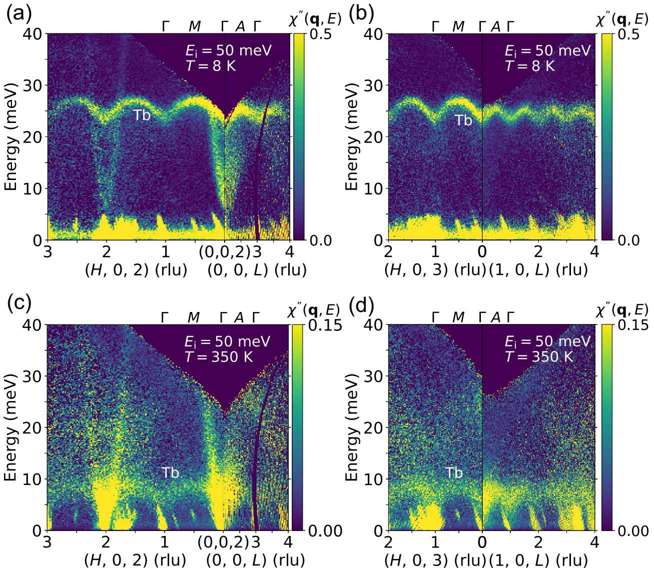

FIG. 2. Magnetic excitation spectra obtained at $T = 8$ and 350 K. (a) and (c) are along [H, 0, 2] and [0, 0, L], while (b) and (d) are along [H, 0, 3] and [1, 0, L], respectively. The integration widths are $\Delta H = \pm 0.2$ rlu, $\Delta K = \pm 0.1$ rlu, and $\Delta L = \pm 0.4$ rlu. The integration ranges were chosen such that the data statistics are optimized, without affecting the intrinsic behavior in our data, e.g., the dispersion.

To gain more insights into the spin-reorientation in $\mathrm{TbMn_6Sn_6}$, we performed INS measurements at 200 K to investigate the temperature evolution of the Tb mode. Since the strong intensity of the Mn even mode might obscure the observation of the Tb band, we plot the dispersion along the [H, 0, 3] and [1, 0, L] directions where the intensity of the Mn even mode is weak. The data collected with $E_\mathrm{i} = 50$ meV are presented in Fig. 3(a). There is a high-energy mode located at about 22 meV, which is close to the mode observed at 8 K, albeit slightly softened. The bandwidth of this mode is about 2 meV, smaller than the 5 meV bandwidth at 8 K. More interestingly, we find that there is also a weak low-energy mode, with a band top below ∼10 meV. To examine this mode in more detail, the data with a lower $E_\mathrm{i} = 21$ meV are shown in Fig. 3(b). The low-energy mode at 200 K disperses from the Γ point, resembling the low-energy mode at 350 K, and exhibits a bandwidth of about 6 meV and a small gap at the Γ point. We further analyzed the data by taking different constant-$\boldsymbol{Q}$ cuts, so as to obtain the intensity as a function of energy transfer. Gaussian functions were used to fit the resulting cuts, from which we extracted the peak positions of the two modes at 200 K. Similar analyses have been applied to the data at 8 and 350 K. The dispersion of the high- and low-energy modes are plotted in Figs. 3(c) and 3(d), respectively, which clearly show that at 200 K there is a coexistence of two distinct modes. Similar observations have also been reported in Ref. [55]. In Fig. 3(d), it is shown that the low-energy mode

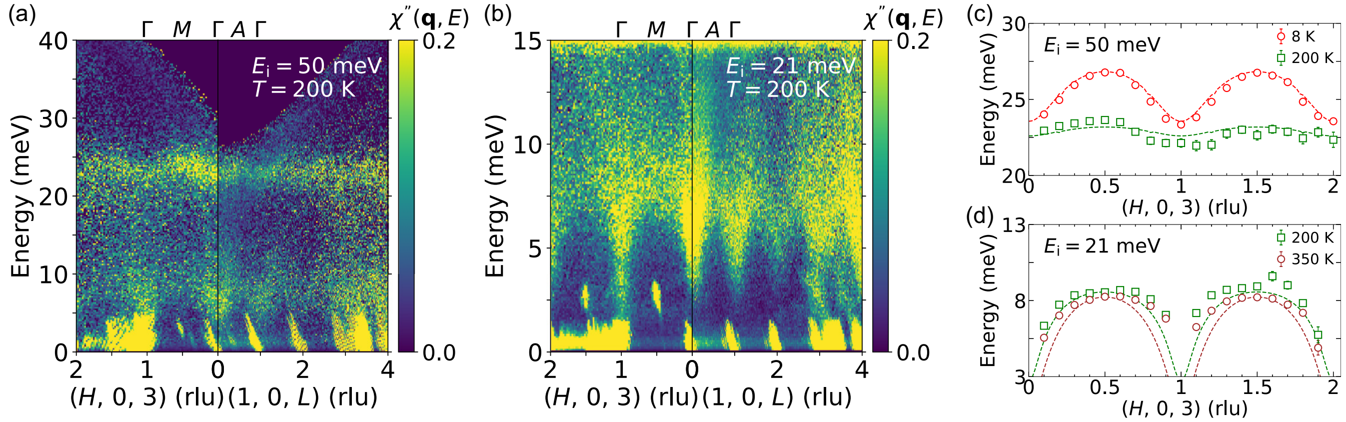

FIG. 3. Magnetic excitation spectra of $\mathrm{TbMn_6Sn_6}$ measured along $[H, 0, 3]$ and $[1, 0, L]$ with integration widths of ΔH of ±0.2 rlu, ΔK of ±0.1 rlu and ΔL of ±0.4 rlu. [(a) and (b)] Spectra measured at 200 K with $E_\mathrm{i} = 50$ and 21 meV, respectively. Comparison between the (c) high-energy modes at 8 and 200 K, and (d) the low-energy modes at 200 and 350 K. Dashed lines are the fits to data, based on the model described in the text. The goodness of fit, defined as $\chi^2 = \sum_i \frac{(\mathrm{THE}_i - \mathrm{EXP}_i)^2}{\mathrm{EXP}_i}$ is 0.06, 1.9, and 5.1 for the data at 8, 200, and 350 K, respectively. THE_i and EXP_i represent data points from theory and experiment, respectively.

at 200 K nearly overlaps with that at 350 K. On the other hand, the high-energy mode is slightly softened, and exhibits a significant bandwidth reduction, compared to the 8-K data.

The experimental observation of the coexistence of two Tb modes at 200 K contradicts the expectation that the evolution of the spin dynamics in $\mathrm{TbMn_6Sn_6}$ upon warming can simply be accounted for by the reduction of spin anisotropy, since in this case only one mode is anticipated. In fact, we were unable to obtain the two modes using linear-spin-wave theory (as implemented in `SpinW` [61]) with the Heisenberg Hamiltonian given in Ref. [44], by tuning the Tb and Mn single-ion anisotropy terms. This indicates that additional mechanisms are needed to capture the spin dynamics of $\mathrm{TbMn_6Sn_6}$ at 200 K, which can also play a key role in driving the spin-reorientation transition.

In Ref. [55], the coexistence of two Tb modes is interpreted as a mixing of the low- and high-temperature states, and the spin-reorientation results from a temperature-induced change of the thermal occupancy of the two states. While this picture accounts for the coexistence of two Tb modes and the spin reorientation, it does not capture the softening and bandwidth reduction of the high-energy mode. Furthermore, the low-energy mode with a small gap at 200 K is also difficult to be reconciled with this picture. Below, we present a model based on SU(N) spin-wave theory that can give rise to these features, and provide an understanding of the temperature evolution of the spin excitations and spin-reorientation process of $\mathrm{TbMn_6Sn_6}$.

B. SU(N) spin-wave simulations

To describe the low-energy modes in the INS spectra, we propose an extended effective spin model to that in Ref. [44],

$$H = H_\mathrm{T} + H_\mathrm{M} + H_\mathrm{MT}, \tag{1}$$

which consists of a term representing the crystal field of the Tb ions (H_T), exchange interactions between Mn ions (H_M), and exchange interactions between neighboring Mn and Tb layers (H_MT). Compared with the spin model proposed in Ref. [44], our approach introduces the crystal field effect of Tb ions and the multipolar interaction between Mn and Tb ions.

In $\mathrm{TbMn_6Sn_6}$, the $\mathrm{Tb^{3+}}$ ion has a $4f^8$ configuration [54], with the lowest-energy manifold of the isolated $\mathrm{Tb^{3+}}$ ions corresponding to ${}^7F_6$ ($L = 3, S = 3$ and $J = 6$). The $\mathrm{Tb^{3+}}$ ions in $\mathrm{TbMn_6Sn_6}$ occupy the $1a$ site with the D_{6h} point group. Therefore, by symmetry analysis, the local crystal field of $\mathrm{Tb^{3+}}$ ions can be written as

$$H_\mathrm{T} = B_2^0 O_2^0 + B_4^0 O_4^0 + B_6^0 O_6^0 + B_6^6\left(O_6^6 + O_6^{-6}\right), \tag{2}$$

where O_l^m are the Stevens operators which can be expressed in terms of the total angular momentum operators of the $\mathrm{Tb^{3+}}$ ions, and B_l^m are the Stevens parameters. The exchange interactions between Mn ions are given by

$$H_\mathrm{M} = \sum_{\langle ij\rangle} J\boldsymbol{S}_i \cdot \boldsymbol{S}_j + \sum_k \sum_{i<j} J_k^\mathrm{MM} \boldsymbol{S}_i \cdot \boldsymbol{S}_{j+k} + \sum_i \left(D_x S_{ix}^2 + D_y S_{iy}^2\right), \tag{3}$$

where J, J_k^MM, and D_x (D_y) are the nearest-neighbor exchange coupling between the Mn ions within the kagome plane, interlayer exchange coupling between Mn ions, and the single-ion anisotropy of Mn ions with spin $S = 1$, respectively. The coupling between Mn and Tb is expressed as

$$H_\mathrm{MT} = \sum_{\langle i<j\rangle} J^\mathrm{MT} \boldsymbol{S}_i \cdot \boldsymbol{J}_j + \sum_{\langle i<j\rangle} J_{zz}^\mathrm{MT} S_{iz}^2 J_{jz}^2, \tag{4}$$

where $\boldsymbol{J}_j$ is the total angular momentum of $\mathrm{Tb^{3+}}$. J_{zz}^MT is a multipolar interaction. From a local spin perspective, the magnetic interactions between Tb and Mn ions can be derived from a multiorbital Hubbard model that includes the orbitals on both Tb and Mn ions. By projecting the multiorbital model onto the low-energy states, it becomes apparent that the magnetic interactions between Tb and Mn ions involve terms beyond the Heisenberg term, primarily owing to the presence of spin-orbital coupling [62]. To simplify the analysis, we will primarily focus on the Heisenberg term J^MT and the multipolar interaction J_{zz}^MT. All the relevant exchange paths

TABLE I. Exchange interactions and Stevens' parameters (in meV) at different temperatures obtained by fitting the INS results.

T (K)	J	J_1^{MM}	J_2^{MM}	J^{MT}	J_{zz}^{MT}	D_x	D_y	B_2^0	$B_4^0(\times 10^{-4})$	$B_6^0(\times 10^{-6})$	B_6^6
8	−28.8	−5.35	−22.4	0.90	−0.2125	−16.50	−16.50	−0.019	7.83	7.98	0
200	−28.8	−5.35	−22.4	0.72	−0.055	−0.50	−1.50	−0.019	7.83	7.98	0
350	−28.8	−5.35	−22.4	0.88	−0.0005	−6.50	−6.50	−0.019	7.83	7.98	0

are shown in Fig. 1(a). Although the Mn spin is typically treated as localized [44,55], the Mn electrons in fact have a strong itinerant character [39,46,48]. Therefore J^{MT} can be viewed as a Kondo coupling between itinerant Mn electrons and localized Tb spins [63].

Since there is a long-range ferrimagnetic order in TbMn$_6$Sn$_6$, we apply spin-wave theory to study its spin dynamics. To facilitate the treatment of excitations between the complex spin-orbital-entangled states, we use SU(N) instead of the SU(2) theory to calculate the excitation spectra [64]. These spectra are determined using the correlation function,

$$S(\boldsymbol{q},\omega)=\frac{1}{2N}\int dte^{-i\omega t}\sum_{\alpha\beta=x,y,z}(\delta_{\alpha\beta}-\hat{q}_\alpha\hat{q}_\beta)\times\sum_{rr'}e^{i\boldsymbol{q}\cdot(\boldsymbol{r}-\boldsymbol{r}')}\langle O_r^\alpha O_{r'}^\beta(t)\rangle, \tag{5}$$

where O^α is the spin (total angular momentum) operator S_α (J_α) for the Mn (Tb) ions. The operators $\boldsymbol{J}_r$ and $\boldsymbol{S}_r$ can be expressed in terms of Schwinger bosons b_{rm}^{Tb} and b_{rm}^{Mn}, respectively. These Schwinger bosons b_m^{Tb} (b_m^{Mn}) correspond to the eigenstates $|m\rangle_{\mathrm{Tb}}$ ($|m\rangle_{\mathrm{Mn}}$) of J_z (S_z). To model the spin reorientation and excitation spectra at different temperatures, we vary the different exchange interactions between the Mn and Tb ions, together with the single-ion anisotropy terms for Mn, as detailed in Table I. The ground states, outlined in Table II, are obtained by solving the ansatz of the Hamiltonian H. The components of the excited states are calculated through the following correlation function

$$N_m^{\mathrm{Tb/Mn}}(\boldsymbol{q},\omega)=\frac{1}{2N}\int dte^{-i\omega t}\times\sum_{rr'}e^{i\boldsymbol{q}\cdot(\boldsymbol{r}-\boldsymbol{r}')}\langle b_{rm}^{\dagger,\mathrm{Tb/Mn}}b_{r'm}^{\mathrm{Tb/Mn}}(t)\rangle, \tag{6}$$

where N is the number of spin-wave modes.

At 8 K, the large coupling J_{zz}^{MT} yields a magnetic moment aligning with the c-axis [Fig. 4(a)]. This means that the ground states of the Tb and Mn ions are the $|m_J=\pm 6\rangle$ and $|m_S=\mp 1\rangle$ states, respectively. The calculated spectra at 8 K are shown in Fig. 4(g), where the Tb mode near 25 meV and the gapped Mn modes are well simulated. Given that the scattered neutrons carry spin-1 excitations, the mode near 25 meV in the spectrum represents the spin-1 excitations from $|-6\rangle$ to $|-5\rangle$, as shown in Fig. 4(d). The gap in the Tb mode primarily arises from the large coupling J_{zz}^{MT}, while the gap in the Mn modes predominantly arises from the combined influence of the J_{zz}^{MT} coupling and the single-ion anisotropy D_x and D_y of the Mn ions. The J_{zz}^{MT} coupling amplifies the gap of the Mn modes, whereas the single-ion anisotropy reduces the gap of the Mn modes when the magnetic moment is aligned along the c axis.

Upon increasing the temperature to 200 K, we maintain the crystal field parameters and couplings between Mn ions, while reducing J^{MT}, J_{zz}^{MT}, D_x, and D_y (Table I). A new state $|\phi_{200\,\mathrm{K}}\rangle$ becomes the ground state for Tb^{3+}, which is induced by the interplay between the crystalline electric field, Mn single-ion anisotropy and exchange interactions between Tb and Mn ions. Under such circumstances, the magnetic moment is tilted away from the c axis towards the ab plane, as illustrated in Fig. 4(b). The corresponding calculated spectrum, illustrated in Fig. 4(h), successfully captures the main features of the experimental data at 200 K (Fig. 3), including an almost flat band around 22 meV, and a small-gap mode with a bandwidth of ~6 meV at low energies. In the excitation spectrum, these two modes correspond to spin-1 excitations from $|\phi_{200\,\mathrm{K}}\rangle$ to the excited states. As shown in Fig. 4(e), the dominant component of the upper excited state is $|-4\rangle$, while the dominant components of the lower excited state are $|-6\rangle$ and $|-5\rangle$. Since the main components of the ground state $|\phi_{200\mathrm{K}}\rangle$ are $|-6\rangle$ and $|-5\rangle$ [see Table II and Fig. 4(e)], the primary contribution to the spin-1 excitation consists of the transitions from $|-6\rangle$ to $|-5\rangle$, $|-5\rangle$ to $|-6\rangle$, and $|-5\rangle$ to $|-4\rangle$, as shown in Fig. 4(e). The low-energy mode results from hybridization between the flat crystal-field excitations of the Tb ions and the dispersive spin waves of the Mn ions. The energy gap in the low-energy mode arises from the differentiation between D_x and D_y of the Mn ions, a distinction that leads to the absence of U(1) symmetry in our model.

At 350 K, above the spin-reorientation transition, we amplify the single-ion anisotropic terms of Mn to enforce in-plane magnetic moments [Fig. 4(c)]. The calculated spectra, as shown in Fig. 4(i), exhibit a low-energy gapless mode dispersing from the Γ point, which is consistent with the experimental results as shown in Fig. 2(d). The dominant components of the ground state of Tb become $|0\rangle$, $|\pm 1\rangle$, and

TABLE II. Ground states of Tb^{3+} in our model in terms of $|m\rangle_{\mathrm{Tb}}$. $|\phi_{8\,\mathrm{K}}\rangle$, $|\phi_{200\,\mathrm{K}}\rangle$, and $|\phi_{350\,\mathrm{K}}\rangle$ correspond to the ground states at 8, 200, and 350 K, respectively.

$|m_J\rangle$	$|6\rangle$	$|5\rangle$	$|4\rangle$	$|3\rangle$	$|2\rangle$	$|1\rangle$	$|0\rangle$	$|-1\rangle$	$|-2\rangle$	$|-3\rangle$	$|-4\rangle$	$|-5\rangle$	$|-6\rangle$
$|\phi_{8\mathrm{K}}\rangle$	0	0	0	0	0	0	0	0	0	0	0	0	1
$|\phi_{200\mathrm{K}}\rangle$	0	0	0	0	0	0	0	0.00006	0.00473	0.03170	0.17376	0.63170	0.75481
$|\phi_{350\mathrm{K}}\rangle$	0.02271	0.08214	0.16367	0.25415	0.34670	0.42261	0.45290	0.42261	0.34670	0.25415	0.16367	0.08214	0.02271

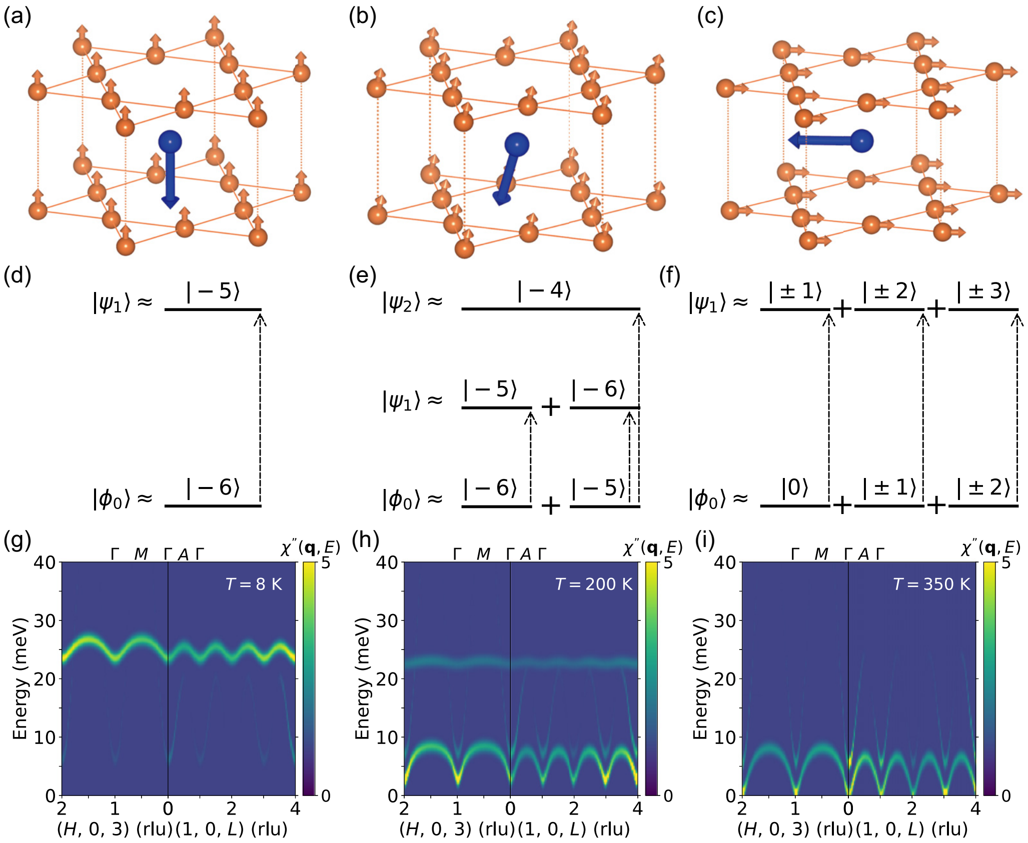

FIG. 4. [(a), (b), and (c)] Magnetic structures of $TbMn_6Sn_6$ at 8, 200, and 350 K, respectively. [(d), (e), and (f)] Diagrams of the dominant spin-1 excitation from the ground state to the excited state at 8, 200, and 350 K, respectively. [(g), (h), and (i)] Calculated spectra at 8, 200, and 350 K, respectively, based on the excitation processes illustrated in the middle row using SU(N) spin-wave theory. We note that the Mn odd modes are too weak to be observed experimentally.

$|\pm2\rangle$, and the primary components of the low-energy excited states around 8 meV become $|\pm1\rangle$, $|\pm2\rangle$, and $|\pm3\rangle$, as shown in Fig. 4(f). Therefore the contributions to the low-energy mode are transitions from $|0\rangle$ to $|\pm1\rangle$, $|\pm1\rangle$ to $|\pm2\rangle$, and $|\pm2\rangle$ to $|\pm3\rangle$. The gaplessness of the low-energy mode is due to the spontaneous symmetry breaking of the U(1) symmetry within the Hamiltonian.

In the calculations, there are hybridization gaps between the acoustic magnon modes resulting from the Mn ions and the bands resulting from the Tb ions, which are not resolved in our experimental data, likely due to instrumental resolution and broadening effects not considered in the calculations.

IV. DISCUSSIONS AND CONCLUSIONS

In this paper, we use elastic neutron scattering to show that there is a spin-reorientation process at ~330 K in $TbMn_6Sn_6$, below which the Tb moment switches from in-plane to out-of-plane. Intriguingly, our INS results show that there are two Tb modes at 200 K. This coexistence was previously accounted for on the basis of a two-orbital model, whereby an excited state becomes increasingly thermally populated with increasing temperature [55], inducing the spin-reorientation process. However, this scenario appears to have difficulties in explaining the two distinct modes at 200 K. Furthermore, calculations for such a scenario based on coupled crystal-electric-field states using random-phase approximations show multiple modes at intermediate energies, which are not observed experimentally. In this work, we provide an alternative microscopic model which can account for the observed temperature evolution of the excitations, whereby the evolution of the Tb mode reflects the temperature dependence of the ground state. This is consistent with the temperature evolution of three magnetically ordered regions evidenced by distinct internal magnetic fields in muon-spin relaxation experiments [45]. Our results show that the two Tb modes at 200 K arise from excitations between a new ground state to its excited state, distinct from those at 8 and 350 K. In our model, the different behaviors of the two modes at 200 K compared to those at 8 and 350 K are understandable.

We show that the combined effect of the crystal field potential, single-ion anisotropy of Mn and couplings between Mn and Tb layers, tunes the ground states and gives rise to the spin reorientation. At low temperatures, the large coupling J_{zz}^{MT} leads to the ground state of $|\pm6\rangle$ for Tb. Since the couplings between Mn and Tb ions decrease with increasing temperature, at high temperatures, the crystal field potential plays a very important role in driving the Tb ground state in which the direction of the magnetic moment deviates from the *c*-axis, and at 350 K a slight change of the single-ion anisotropy reorients the magnetic moments to the *ab* plane. Our model provides a plausible mechanism for the spin-reorientation process, which is key to realizing the topological electronic states at low temperatures [46]. Our findings also underscore the important role of interactions between the crystal field and the magnetic couplings. Interestingly, the coupling between the localized Tb 4f moments and the itinerant Mn d electrons is very similar to the Kondo effect widely discussed in heavy-fermion systems with f electrons [65]. It is noteworthy that the Kondo effect in d-electron systems has also been found in recent years [63,66,67], suggesting the applicability of Kondo physics to broader classes of condensed matter systems.

ACKNOWLEDGMENTS

The work was supported by National Key Projects for Research and Development of China with Grants No. 2021YFA1400400 and No. 2022YFA1402200, National Natural Science Foundation of China with Grants No. 12225407, 12074174, 12074175, 12004191, 12274363, 12222410, and 12174332, Natural Science Foundation of Jiangsu province with Grant No. BK20200738, Natural Science Foundation of the Higher Education Institutions of Jiangsu Province with Grant No. 23KJB140012, China Postdoctoral Science Foundation with Grants No. 2022M711569 and No. 2022T150315, Jiangsu Province Excellent Postdoctoral Program with Grant No. 20220ZB5, Natural Science Research Start-up Foundation of Posts and Telecommunications with Grant No. NY220095, the Pioneer and Leading Goose R&D Program of Zhejiang (2022SDXHDX0005), the Key R&D Program of Zhejiang Province, China (2021C01002), and Fundamental Research Funds for the Central Universities. We acknowledge the neutron beam time from J-PARC with Proposal Nos. 2021B0111 and 2021B0207 and from ANSTO with Proposal No. 9792.

---

[1] J. Wen, S.-L. Yu, S. Li, W. Yu, and J.-X. Li, Experimental identification of quantum spin liquids, npj Quantum Mater. **4**, 12 (2019).

[2] C. Broholm, R. J. Cava, S. A. Kivelson, D. G. Nocera, M. R. Norman, and T. Senthil, Quantum spin liquids, Science **367**, eaay0668 (2020).

[3] N. J. Ghimire and I. I. Mazin, Topology and correlations on the kagome lattice, Nat. Mater. **19**, 137 (2020).

[4] J.-X. Yin, B. Lian, and M. Z. Hasan, Topological kagome magnets and superconductors, Nature (London) **612**, 647 (2022).

[5] I. I. Mazin, H. O. Jeschke, F. Lechermann, H. Lee, M. Fink, R. Thomale, and R. Valentí, Theoretical prediction of a strongly correlated Dirac metal, Nat. Commun. **5**, 4261 (2014).

[6] K. Kuroda, T. Tomita, M. T. Suzuki, C. Bareille, A. A. Nugroho, P. Goswami, M. Ochi, M. Ikhlas, M. Nakayama, S. Akebi, R. Noguchi, R. Ishii, N. Inami, K. Ono, H. Kumigashira, A. Varykhalov, T. Muro, T. Koretsune, R. Arita, S. Shin *et al.*, Evidence for magnetic Weyl fermions in a correlated metal, Nat. Mater. **16**, 1090 (2017).

[7] X. Li, L. Xu, L. Ding, J. Wang, M. Shen, X. Lu, Z. Zhu, and K. Behnia, Anomalous Nernst and Righi-Leduc effects in Mn_3Sn: Berry curvature and entropy flow, Phys. Rev. Lett. **119**, 056601 (2017).

[8] M. Kang, L. Ye, S. Fang, J.-S. You, A. Levitan, M. Han, J. I. Facio, C. Jozwiak, A. Bostwick, E. Rotenberg, M. K. Chan, R. D. McDonald, D. Graf, K. Kaznatcheev, E. Vescovo, D. C. Bell, E. Kaxiras, J. v. d. Brink, M. Richter, M. P. Ghimire *et al.*, Dirac fermions and flat bands in the ideal kagome metal FeSn, Nat. Mater. **19**, 163 (2020).

[9] D. F. Liu, A. J. Liang, E. K. Liu, Q. N. Xu, Y. W. Li, C. Chen, D. Pei, W. J. Shi, S. K. Mo, P. Dudin, T. Kim, C. Cacho, G. Li, Y. Sun, L. X. Yang, Z. K. Liu, S. S. P. Parkin, C. Felser, and Y. L. Chen, Magnetic Weyl semimetal phase in a Kagomé crystal, Science **365**, 1282 (2019).

[10] N. Morali, R. Batabyal, P. K. Nag, E. Liu, Q. Xu, Y. Sun, B. Yan, C. Felser, N. Avraham, and H. Beidenkopf, Fermi-arc diversity on surface terminations of the magnetic Weyl semimetal $Co_3Sn_2S_2$, Science **365**, 1286 (2019).

[11] R. Chisnell, J. S. Helton, D. E. Freedman, D. K. Singh, R. I. Bewley, D. G. Nocera, and Y. S. Lee, Topological magnon bands in a kagome lattice ferromagnet, Phys. Rev. Lett. **115**, 147201 (2015).

[12] A. Mook, J. Henk, and I. Mertig, Edge states in topological magnon insulators, Phys. Rev. B **90**, 024412 (2014).

[13] S.-L. Yu and J.-X. Li, Chiral superconducting phase and chiral spin-density-wave phase in a Hubbard model on the kagome lattice, Phys. Rev. B **85**, 144402 (2012).

[14] B. R. Ortiz, S. M. L. Teicher, Y. Hu, J. L. Zuo, P. M. Sarte, E. C. Schueller, A. M. M. Abeykoon, M. J. Krogstad, S. Rosenkranz, R. Osborn, R. Seshadri, L. Balents, J. He, and S. D. Wilson, CsV_3Sb_5: A $\mathbb{Z}_2$ Topological kagome metal with a superconducting ground state, Phys. Rev. Lett. **125**, 247002 (2020).

[15] J.-X. Yin, S. S. Zhang, G. Chang, Q. Wang, S. S. Tsirkin, Z. Guguchia, B. Lian, H. Zhou, K. Jiang, I. Belopolski, N. Shumiya, D. Multer, M. Litskevich, T. A. Cochran, H. Lin, Z. Wang, T. Neupert, S. Jia, H. Lei, and M. Z. Hasan, Negative flat band magnetism in a spin-orbit-coupled correlated kagome magnet, Nat. Phys. **15**, 443 (2019).

[16] W. R. Meier, M.-H. Du, S. Okamoto, N. Mohanta, A. F. May, M. A. McGuire, C. A. Bridges, G. D. Samolyuk, and B. C. Sales, Flat bands in the CoSn-type compounds, Phys. Rev. B **102**, 075148 (2020).

[17] Z. Liu, M. Li, Q. Wang, G. Wang, C. Wen, K. Jiang, X. Lu, S. Yan, Y. Huang, D. Shen, J.-X. Yin, Z. Wang, Z. Yin, H. Lei, and S. Wang, Orbital-selective Dirac fermions and extremely flat bands in frustrated kagome-lattice metal CoSn, Nat. Commun. **11**, 4002 (2020).

[18] M. Kang, S. Fang, L. Ye, H. C. Po, J. Denlinger, C. Jozwiak, A. Bostwick, E. Rotenberg, E. Kaxiras, J. G. Checkelsky, and R. Comin, Topological flat bands in frustrated kagome lattice CoSn, Nat. Commun. **11**, 4004 (2020).

[19] Y.-X. Jiang, J.-X. Yin, M. M. Denner, N. Shumiya, B. R. Ortiz, G. Xu, Z. Guguchia, J. He, M. S. Hossain, X. Liu, J. Ruff, L. Kautzsch, S. S. Zhang, G. Chang, I. Belopolski, Q. Zhang, T. A. Cochran, D. Multer, M. Litskevich, Z.-J. Cheng *et al.*,

Unconventional chiral charge order in kagome superconductor KV_3Sb_5, Nat. Mater. **20**, 1353 (2021).

[20] H. Li, T. T. Zhang, T. Yilmaz, Y. Y. Pai, C. E. Marvinney, A. Said, Q. W. Yin, C. S. Gong, Z. J. Tu, E. Vescovo, C. S. Nelson, R. G. Moore, S. Murakami, H. C. Lei, H. N. Lee, B. J. Lawrie, and H. Miao, Observation of unconventional charge density wave without acoustic phonon anomaly in kagome superconductors AV_3Sb_5 (A = Rb, Cs), Phys. Rev. X **11**, 031050 (2021).

[21] X. Teng, L. Chen, F. Ye, E. Rosenberg, Z. Liu, J.-X. Yin, Y.-X. Jiang, J. S. Oh, M. Z. Hasan, K. J. Neubauer, B. Gao, Y. Xie, M. Hashimoto, D. Lu, C. Jozwiak, A. Bostwick, E. Rotenberg, R. J. Birgeneau, J.-H. Chu, M. Yi *et al.*, Discovery of charge density wave in a kagome lattice antiferromagnet, Nature (London) **609**, 490 (2022).

[22] Z. Lin, J.-H. Choi, Q. Zhang, W. Qin, S. Yi, P. Wang, L. Li, Y. Wang, H. Zhang, Z. Sun, L. Wei, S. Zhang, T. Guo, Q. Lu, J.-H. Cho, C. Zeng, and Z. Zhang, Flatbands and emergent ferromagnetic ordering in Fe_3Sn_2 kagome lattices, Phys. Rev. Lett. **121**, 096401 (2018).

[23] S. Cao, C. Xu, H. Fukui, T. Manjo, M. Shi, Y. Liu, C. Cao, and Y. Song, Competing charge-density wave instabilities in the kagome metal ScV_6Sn_6, Nat. Commun. **14**, 7671 (2023).

[24] T. Kida, L. A. Fenner, A. A. Dee, I. Terasaki, M. Hagiwara, and A. S. Wills, The giant anomalous Hall effect in the ferromagnet Fe_3Sn_2 —a frustrated kagome metal, J. Phys.: Condens. Matter **23**, 112205 (2011).

[25] G. Xu, B. Lian, and S.-C. Zhang, Intrinsic quantum anomalous Hall effect in the kagome lattice $Cs_2LiMn_3F_{12}$, Phys. Rev. Lett. **115**, 186802 (2015).

[26] Q. Wang, S. Sun, X. Zhang, F. Pang, and H. Lei, Anomalous Hall effect in a ferromagnetic Fe_3Sn_2 single crystal with a geometrically frustrated Fe bilayer kagome lattice, Phys. Rev. B **94**, 075135 (2016).

[27] S. Nakatsuji, N. Kiyohara, and T. Higo, Large anomalous Hall effect in a non-collinear antiferromagnet at room temperature, Nature (London) **527**, 212 (2015).

[28] E. Liu, Y. Sun, N. Kumar, L. Muechler, A. Sun, L. Jiao, S.-Y. Yang, D. Liu, A. Liang, Q. Xu, J. Kroder, V. Süß, H. Borrmann, C. Shekhar, Z. Wang, C. Xi, W. Wang, W. Schnelle, S. Wirth, Y. Chen *et al.*, Giant anomalous Hall effect in a ferromagnetic kagome-lattice semimetal, Nat. Phys. **14**, 1125 (2018).

[29] Q. Wang, Y. Xu, R. Lou, Z. Liu, M. Li, Y. Huang, D. Shen, H. Weng, S. Wang, and H. Lei, Large intrinsic anomalous Hall effect in half-metallic ferromagnet $Co_3Sn_2S_2$ with magnetic Weyl fermions, Nat. Commun. **9**, 3681 (2018).

[30] Q. Wang, K. J. Neubauer, C. Duan, Q. Yin, S. Fujitsu, H. Hosono, F. Ye, R. Zhang, S. Chi, K. Krycka, H. Lei, and P. Dai, Field-induced topological Hall effect and double-fan spin structure with a c-axis component in the metallic kagome antiferromagnetic compound YMn_6Sn_6, Phys. Rev. B **103**, 014416 (2021).

[31] T. Asaba, S. M. Thomas, M. Curtis, J. D. Thompson, E. D. Bauer, and F. Ronning, Anomalous Hall effect in the kagome ferrimagnet $GdMn_6Sn_6$, Phys. Rev. B **101**, 174415 (2020).

[32] N. J. Ghimire, R. L. Dally, L. Poudel, D. C. Jones, D. Michel, N. T. Magar, M. Bleuel, M. A. McGuire, J. S. Jiang, J. F. Mitchell, J. W. Lynn, and I. I. Mazin, Competing magnetic phases and fluctuation-driven scalar spin chirality in the kagome metal YMn_6Sn_6, Sci. Adv. **6**, eabe2680 (2020).

[33] M. Li, Q. Wang, G. Wang, Z. Yuan, W. Song, R. Lou, Z. Liu, Y. Huang, Z. Liu, H. Lei, Z. Yin, and S. Wang, Dirac cone, flat band and saddle point in kagome magnet YMn_6Sn_6, Nat. Commun. **12**, 3129 (2021).

[34] M. Dirken, R. Thiel, J. Brabers, F. de Boer, and K. Buschow, ^{155}Gd Mössbauer effect and magnetic properties of $GdMn_6Sn_6$, J. Alloys Compd. **177**, L11 (1991).

[35] B. El Idrissi, G. Venturini, B. Malaman, and D. Fruchart, Magnetic structures of $TbMn_6Sn_6$ and $HoMn_6Sn_6$ compounds from neutron diffraction study, J. Less-Common Met. **175**, 143 (1991).

[36] B. Malaman, G. Venturini, R. Welter, J. Sanchez, P. Vulliet, and E. Ressouche, Magnetic properties of RMn_6Sn_6 (R=Gd-Er) compounds from neutron diffraction and Mössbauer measurements, J. Magn. Magn. **202**, 519 (1999).

[37] G. Venturini, R. Welter, B. Malaman, and E. Ressouche, Magnetic structure of YMn_6Ge_6 and room temperature magnetic structure of $LuMn_6Sn_6$ obtained from neutron diffraction study, J. Alloys Compd. **200**, 51 (1993).

[38] G. Venturini, D. Fruchart, and B. Malaman, Incommensurate magnetic structures of RMn_6Sn_6(R = Sc, Y, Lu) compounds from neutron diffraction study, J. Alloys Compd. **236**, 102 (1996).

[39] W. Ma, X. Xu, J.-X. Yin, H. Yang, H. Zhou, Z.-J. Cheng, Y. Huang, Z. Qu, F. Wang, M. Z. Hasan, and S. Jia, Rare earth engineering in $R\mathrm{Mn}_6\mathrm{Sn}_6$ (R = Gd−Tm, Lu) topological kagome magnets, Phys. Rev. Lett. **126**, 246602 (2021).

[40] H. Zhang, X. Feng, T. Heitmann, A. I. Kolesnikov, M. B. Stone, Y.-M. Lu, and X. Ke, Topological magnon bands in a room-temperature kagome magnet, Phys. Rev. B **101**, 100405(R) (2020).

[41] G. Venturini, B. C. El Idrissi, and B. Malaman, Magnetic properties of RMn_6Sn_6 (R = Sc, Y, Gd-Tm, Lu) compounds with $HfFe_6Ge_6$ type structure, J. Magn. Magn. **94**, 35 (1991).

[42] D. M Clatterbuck and K. Gschneidner, Jr., Magnetic properties of RMn_6Sn_6 (R=Tb, Ho, Er, Tm, Lu) single crystals, J. Magn. Magn. Mater. **207**, 78 (1999).

[43] N. Zajkov, N. Mushnikov, M. Bartashevich, and T. Goto, Magnetization processes in the $TbMn_6Sn_6$ compound, J. Alloys Compd. **309**, 26 (2000).

[44] S. X. M. Riberolles, T. J. Slade, D. L. Abernathy, G. E. Granroth, B. Li, Y. Lee, P. C. Canfield, B. G. Ueland, L. Ke, and R. J. McQueeney, Low-temperature competing magnetic energy scales in the topological ferrimagnet $TbMn_6Sn_6$, Phys. Rev. X **12**, 021043 (2022).

[45] C. Mielke III, W. L. Ma, V. Pomjakushin, O. Zaharko, S. Sturniolo, X. Liu, V. Ukleev, J. S. White, J. X. Yin, S. S. Tsirkin, C. B. Larsen, T. A. Cochran, M. Medarde, V. Porée, D. Das, R. Gupta, C. N. Wang, J. Chang, Z. Q. Wang, R. Khasanov *et al.*, Low-temperature magnetic crossover in the topological kagome magnet $TbMn_6Sn_6$, Commun. Phys. **5**, 107 (2022).

[46] J. X. Yin, W. Ma, T. A. Cochran, X. Xu, S. S. Zhang, H. J. Tien, N. Shumiya, G. Cheng, K. Jiang, B. Lian, Z. Song, G. Chang, I. Belopolski, D. Multer, M. Litskevich, Z. J. Cheng, X. P. Yang, B. Swidler, H. Zhou, H. Lin *et al.*, Quantum-limit Chern topological magnetism in $TbMn_6Sn_6$, Nature (London) **583**, 533 (2020).

[47] H. Zhang, J. Koo, C. Xu, M. Sretenovic, B. Yan, and X. Ke, Exchange-biased topological transverse thermoelectric effects in a kagome ferrimagnet, Nat. Commun. **13**, 1091 (2022).

[48] X. Xu, J.-X. Yin, W. Ma, H.-J. Tien, X.-B. Qiang, P. S. Reddy, H. Zhou, J. Shen, H.-Z. Lu, T.-R. Chang *et al.*, Topological charge-entropy scaling in kagome chern magnet $TbMn_6Sn_6$, Nat. Commun. **13**, 1197 (2022).

[49] N. Zaikov, A. Pirogov, N. Mushnikov, A. Teplykh, E. Valiev, and Y. A. Dorofeev, Magnetic-field-induced spin-reorientational transition in $TbMn_6Sn_6$, JETP Lett. **72**, 436 (2000).

[50] F. D. M. Haldane, Model for a quantum Hall effect without Landau levels: Condensed-matter realization of the "parity anomaly", Phys. Rev. Lett. **61**, 2015 (1988).

[51] V. Y. Irkhin, A new mechanism of first-order magnetization in multisublattice rare-earth compounds, J. Phys.: Condens. Matter **14**, 6865 (2002).

[52] G.-H. Guo and H.-B. Zhang, The spin reorientation transition and first-order magnetization process of $TbMn_6Sn_6$ compound, J. Alloys Compd. **448**, 17 (2008).

[53] E. Rosenfeld and N. Mushnikov, Double-flat-spiral magnetic structures: Theory and application to the RMn_6X_6 compounds, Phys. B **403**, 1898 (2008).

[54] D. C. Jones, S. Das, H. Bhandari, X. Liu, P. Siegfried, M. P. Ghimire, S. S. Tsirkin, I. I. Mazin, and N. J. Ghimire, Origin of spin reorientation and intrinsic anomalous Hall effect in the kagome ferrimagnet $TbMn_6Sn_6$, arXiv:2203.17246 [cond-mat.str-el].

[55] S. X. M. Riberolles, T. J. Slade, R. L. Dally, P. M. Sarte, B. Li, T. Han, H. Lane, C. Stock, H. Bhandari, N. J. Ghimire, D. L. Abernathy, P. C. Canfield, J. W. Lynn, B. G. Ueland, and R. J. McQueeney, Orbital character of the spin-reorientation transition in $TbMn_6Sn_6$, Nat. Commun. **14**, 2658 (2023).

[56] K. Momma and F. Izumi, VESTA 3 for three-dimensional visualization of crystal, volumetric and morphology data, J. Appl. Crystallogr. **44**, 1272 (2011).

[57] P. C. Canfield, T. Kong, U. S. Kaluarachchi, and N. H. Jo, Use of frit-disc crucibles for routine and exploratory solution growth of single crystalline samples, Philos. Mag. **96**, 84 (2016).

[58] R. Kajimoto, M. Nakamura, Y. Inamura, F. Mizuno, K. Nakajima, S. Ohira-Kawamura, T. Yokoo, T. Nakatani, R. Maruyama, K. Soyama, K. Shibata, K. Suzuya, S. Sato, K. Aizawa, M. Arai, S. Wakimoto, M. Ishikado, S.-i. Shamoto, M. Fujita, H. Hiraka *et al.*, The Fermi Chopper spectrometer 4SEASONS at J-PARC, J. Phys. Soc. Jpn. **80**, SB025 (2011).

[59] M. Nakamura, R. Kajimoto, Y. Inamura, F. Mizuno, M. Fujita, T. Yokoo, and M. Arai, First demonstration of novel method for inelastic neutron scattering measurement utilizing multiple incident energies, J. Phys. Soc. Jpn. **78**, 093002 (2009).

[60] R. Ewings, A. Buts, M. Le, J. van Duijn, I. Bustinduy, and T. Perring, Horace: Software for the analysis of data from single crystal spectroscopy experiments at time-of-flight neutron instruments, Nucl. Instrum. Methods Phys. Res., Sect. A **834**, 132 (2016).

[61] S. Toth and B. Lake, Linear spin wave theory for single-Q incommensurate magnetic structures, J. Phys.: Condens. Matter. **27**, 166002 (2015).

[62] P. Santini, S. Carretta, G. Amoretti, R. Caciuffo, N. Magnani, and G. H. Lander, Multipolar interactions in f-electron systems: The paradigm of actinide dioxides, Rev. Mod. Phys. **81**, 807 (2009).

[63] S. Bao, W. Wang, Y. Shangguan, Z. Cai, Z.-Y. Dong, Z. Huang, W. Si, Z. Ma, R. Kajimoto, K. Ikeuchi, S.-i. Yano, S.-L. Yu, X. Wan, J.-X. Li, and J. Wen, Neutron Spectroscopy Evidence on the Dual Nature of Magnetic Excitations in a van der Waals Metallic Ferromagnet $Fe_{2.72}GeTe_2$, Phys. Rev. X **12**, 011022 (2022).

[64] Z.-Y. Dong, W. Wang, and J.-X. Li, SU(N) spin-wave theory: Application to spin-orbital Mott insulators, Phys. Rev. B **97**, 205106 (2018).

[65] G. R. Stewart, Heavy-fermion systems, Rev. Mod. Phys. **56**, 755 (1984).

[66] Y. Zhang, H. Lu, X. Zhu, S. Tan, W. Feng, Q. Liu, W. Zhang, Q. Chen, Y. Liu, X. Luo, D. Xie, L. Luo, Z. Zhang, and X. Lai, Emergence of Kondo lattice behavior in a van der Waals itinerant ferromagnet, Fe_3GeTe_2, Sci. Adv. **4**, eaao6791 (2018).

[67] M. Zhao, B.-B. Chen, Y. Xi, Y. Zhao, H. Xu, H. Zhang, N. Cheng, H. Feng, J. Zhuang, F. Pan, X. Xu, W. Hao, W. Li, S. Zhou, S. X. Dou, and Y. Du, Kondo Holes in the two-dimensional itinerant ising ferromagnet Fe_3GeTe_2, Nano Lett. **21**, 6117 (2021).